Fast Auroral Snapshot observations of perpendicular DC electric field structures in downward auroral current regions: Morphology

K.-J. Hwang,[1] K. A. Lynch,[1] C. W. Carlson,[2] J. W. Bonnell,[2] and W. J. Peria[3]

Received 12 October 2005; revised 13 April 2006; accepted 15 May 2006; published 15 September 2006.

[1] We present an analysis of Fast Auroral Snapshot perpendicular electric field observations using both ion distributions and electric field measurements in auroral downward current regions to study the full DC $\mathbf{E}_\perp$ (electric field perpendicular to the geomagnetic field) and potential structures. We use the electric field data from the field instrument for the spin-plane component of $\mathbf{E}_\perp$, and the ion drift measurements for the axial DC $\mathbf{E}_\perp$. Examining 71 return current region crossings, a significant fraction (more than half) show $\mathbf{E}_\perp$ signatures during strong field events indicative of curved potential structures rather than idealized straight arcs. We define sheetlike structured events as those for which the ratio of the two $\mathbf{E}_\perp$ components remains constant during the spacecraft crossing, and curved structures as those where the ratio varies. Sheetlike structures can be interpreted as straight arcs, but curved structures require gradients in another dimension. A statistical comparison shows parametric differences between sheetlike and curved structures; however, the distinction between sheetlike and curved events cannot be sorted clearly using $\mathbf{j}_\parallel$, $\mathbf{E}_\perp$, or scale length. Using the full DC electric field vector, we can investigate the morphology of auroral return current potential structures and inconsistencies with idealized static return current models. In this paper we present the observed spatial structures; in a companion paper we explore the implications of these observations.

Citation: Hwang, K.-J., K. A. Lynch, C. W. Carlson, J. W. Bonnell, and W. J. Peria (2006), Fast Auroral Snapshot observations of perpendicular DC electric field structures in downward auroral current regions: Morphology, *J. Geophys. Res.*, *111*, A09205, doi:10.1029/2005JA011471.

1. Introduction

[2] The Fast Auroral Snapshot (FAST) satellite investigates auroral physics processes occurring in the boundary region between the collisional ionosphere and the collisionless low-altitude magnetosphere. This region contains electric field formation, particle acceleration, wave-particle interactions, and electromagnetic energy transfer. Auroral current systems participate in global ionosphere-magnetosphere current circuits through field-aligned currents.

[3] These field-aligned currents categorize observations of plasma phenomena in the auroral zone into upward current and downward current regions [*Carlson et al.*, 1998a]. In the downward current region, FAST observes intense upgoing beams of field-aligned electrons of energies of up to several keV, diverging electric fields, and VLF saucers associated with the upgoing electron beams [*Carlson et al.*, 1998b]. Although properties of the downward current system have been discovered by earlier satellites and interpreted as inverse or black aurora, the region has been less explored than upward current regions. In this paper we explore electric fields in the return (downward) current regions and their corresponding potential structures.

[4] The Swedish satellite Freja was launched in 1992 with apogee at 1760 km, well below the lower boundary of the auroral acceleration region. It observed very intense (of the order of 1 V/m) and narrow (a few kilometers) diverging $\mathbf{E}_\perp$ (electric field in the plane perpendicular to the geomagnetic field, $\mathbf{B_0}$) in the midnight and early morning sector. These intense fields were accompanied by upward energetic electron fluxes of typical energies between 100 eV to 1 keV adjacent to the aurora [*Marklund et al.*, 1997]. From these measurements, positive potential structures were predicted to form the counterpart to the negative potential structures of visible aurora [*Marklund et al.*, 1997]. However, Freja's low-altitude passage and poor coverage of pitch angle prevented more conclusive studies.

[5] One of the most significant achievements from FAST, launched in 1996 to higher altitudes near 4000 km, was

[1]Department of Physics and Astronomy, Dartmouth College, Hanover, New Hampshire, USA.
[2]Space Sciences Laboratory, University of California, Berkeley, California, USA.
[3]Department of Geophysics, University of Washington, Seattle, Washington, USA.

0148-0227/06/2005JA011471$09.00

conclusive evidence to confirm the positive potential picture. The intense diverging $\mathbf{E}_\perp$ are observed in return current regions by FAST, but extensive DC $\mathbf{E}_\perp$ morphology studies have not been made with FAST data mainly because of the difficulty of acquiring both orthogonal components of $\mathbf{E}_\perp$. In this paper we use ion moments for the axial $\mathbf{E}_\perp$.

[6] FAST data has high time resolution but is a single spacecraft and thus has an ambiguity for discerning spatial variations from temporal variations. Cluster, launched in 2000, is multispacecraft and can address this ambiguity [*Marklund et al.*, 2001]. Electric field structures associated with the downward current region are seen to have both unipolar [*Karlsson et al.*, 2004] and bipolar [*Marklund et al.*, 2001] signatures and their temporal evolution can be studied. These Cluster signatures are interpreted as the high-altitude analogues of the intense return current auroral electric field structures observed at low altitudes. These observations showed formation and growth time scales of around a few hundred seconds, i.e., almost quasi-static. This time period is comparable to the time needed to evacuate ionospheric electrons over the downward current region, which is supported by numerical simulations [*Marklund et al.*, 2001].

[7] Studies of the self-consistent $\mathbf{E}_\parallel$ in return current regions have been done using a collisionless model of hot anisotropic magnetospheric particles [*Chiu and Schultz*, 1978], using anomalous transport [*Ganguli and Palmadesso*, 1988], using a kinetic model assuming BBELF waves on the finite flux tube heating ions [*Jasperse*, 1998], and using weak electrostatic double layers associated with VLF saucers [*Ergun*, 2001, 2003]. These models describe parallel electic field formation, but provide few details about $\mathbf{E}_\perp$. Numerical simulations about auroral electrodynamics with current and voltage generators [*Lysak*, 1985] concluded that small-scale auroral arcs with bipolar $\mathbf{E}_\perp$ signatures, i.e., V-shaped potential structures, were more likely to be associated with current than voltage generators. These numerical results were made based on two dimensional codes which cannot describe the three dimensional mophology of potential structures in auroral acceleration regions, motivating us to revisit satellite observations.

[8] All these previous studies of downward current region structures assumed black auroral arcs as idealized straight arcs of which perpendicular electric fields, i.e., gradients of potentials, are aligned in only one direction. We present FAST observations showing that in return current regions, curved arcs, for which perpendicular electric fields change their directions along the observational track, are more frequently observed than straight arcs.

[9] The overview of this paper is as follows. This paper is motivated by the fact that DC $\mathbf{E}_\perp$ morphology studies have not been made with FAST data, beginning with a method for extracting two perpendicular components of electric field from FAST data. The ultimate goal of this study is to examine the full DC $\mathbf{E}_\perp$ structures in the return current region, and use them to study the morphology, structure and electrodynamic processes of auroral return currents statistically and by case studies. The statistical analysis was based on 71 events where strong $\mathbf{E}_\perp$ events occur from 50 FAST orbits, mostly comprised of higher time-resolution burst data. Two different types of $\mathbf{E}_\perp$ structures and their corresponding topological studies and differences in magnitude, scale length, current sheet structure, and spatiotemporal properties will be discussed. This paper focuses on the importance of curved structures in return current regions. In a companion paper [*Hwang et al.*, 2006], we present a new interpretation for potential structures in downward current regions that includes ionospheric fields. This new model fits our observations better than the classical U-shaped potential structure.

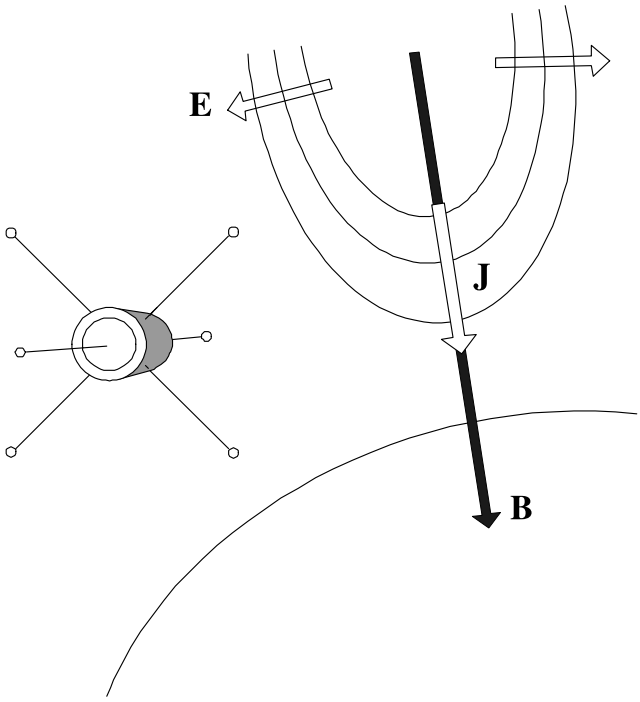

Figure 1. FAST spacecraft trajectory, which is normal to its spin axis, crossing a downward current region.

2. Method

[10] The FAST satellite is an orbit-normal spinner (Figure 1). It has one spin-axial boom which is normal to its orbit, being deployed roughly east-west during FAST's northward or southward crossings of the auroral oval, and two radial wire boom pairs that are in the spin plane. The $\mathbf{E}_\perp$ component which is in the FAST spin plane and along the FAST trajectory is routinely obtained from FAST field data. While the axial boom measurement is available, its interpretation requires careful use and some assumptions. However, moments from the ion data allow us to reconstruct the axial field component. Thus our new method provides an independent measure of this axial component in substitute for the less available axial electric field data. It extracts two perpendicular components of electric field, using the electric field data from the field instrument for the spin-plane component of $\mathbf{E}$, and the ion drift measurements for the axial DC $\mathbf{E}$.

[11] The component of plasma bulk flow in the aperture plane of the ion instrument can be calculated by computing the first moment of the ion velocity distribution function. The ion detectors used do not discriminate between masses, so we must assume a dominant species. Here oxygen was assumed to be the dominant population at the FAST altitude.

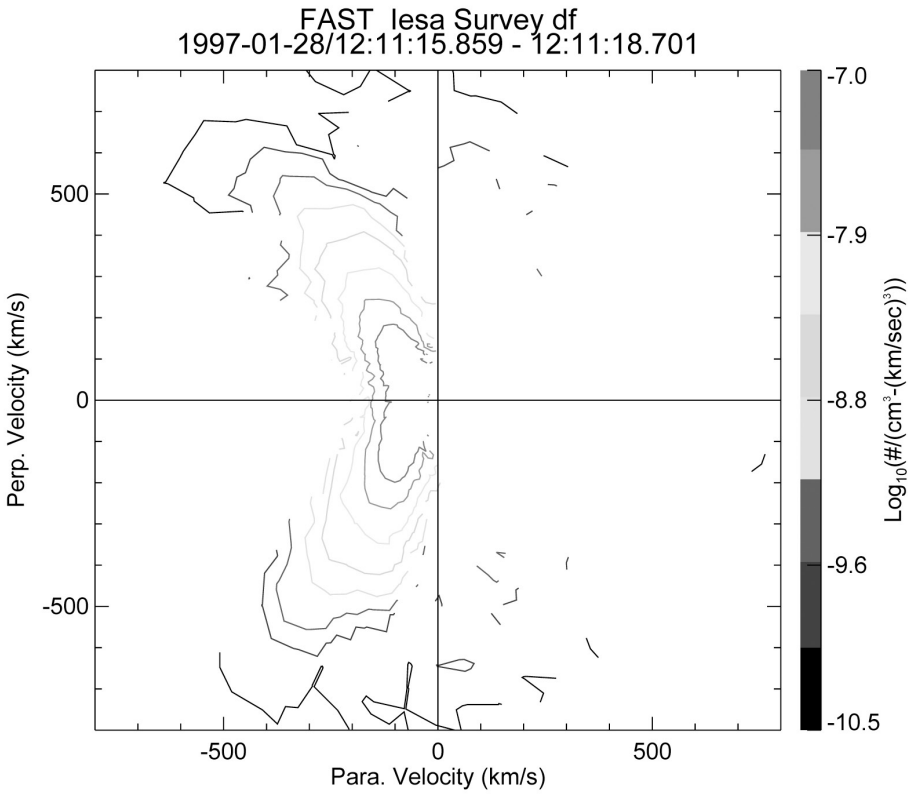

Figure 2. Ion distribution function contours as a function of **v** perpendicular and parallel to the geomagnetic field $\mathbf{B_0}$ during an event of intense ion energy and ion pitch angle asymmetry, from *Lynch et al.* [2002].

In the presence of a background magnetic field, the electric field component perpendicular to both the background magnetic field and ion bulk flow velocity can be calculated assuming an ideal MHD approximation ($\mathbf{E} = -\mathbf{v} \times \mathbf{B}$). Note that the spacecraft ram velocity is included in the ion bulk velocities obtained from the ion distribution function moments.

[12] Thus the ion drift velocity (plasma flow) in the Earth's inertial frame is the vector sum of the velocity measured in the spacecraft frame and the spacecraft velocity. The choice of oxygen as the dominant population gives the best match to the spacecraft velocity in quiet times.

[13] The ideal MHD approximation assumes that the pressure gradient term in the force balance equation is insignificant. We have considered the relative effects of $-\nabla p$ signatures as calculated from the heated ion signatures. The majority of events studied here show $-\nabla p$ signatures of less than 0.1 of the measured electric field signature, with 70 percent of the events having $-\nabla p$ with negligible values (0.05 of measured $q\mathbf{E}_\perp$), and only four examples showing significant fraction of pressure gradient contributions (0.5–0.9 of measured $q\mathbf{E}_\perp$). This analysis of the pressure gradient effect implies that pressure gradients are a secondary effect rather than a driver in these cases. At higher altitudes such as Cluster satellite altitudes, the situation may change, since ion temperatures continuously increase as they move upward along the field lines. When ion populations are further heated, the gradients of pressure may have more significance [*Johansson and Marklund*, 2005].

[14] The ion distribution function patterns in return current regions have various typical conic structures. Figure 2 shows an example of a typical ion distribution function in the return current region, termed an ion conic structure. The distribution has a fairly well-defined pitch angle, but the apex of the conic is offset from the center in the spacecraft frame. We see that the distributions are often nongyrotropic in the payload frame especially during intense diverging $\mathbf{E}_\perp$ events [*Lynch et al.*, 2002]. This perpendicular offset is caused by the ion drift velocity in the plane perpendicular to the magnetic field in the spacecraft frame. After subtracting the spacecraft velocity contribution from the observed ion drift velocity, $\mathbf{v_{measured}} = \mathbf{v_{drift}} - \mathbf{v_{sc}}$ ($\mathbf{v_{drift}}$: the ion drift velocity in the Earth's inertial frame, $\mathbf{v_{measured}}$: the velocity measured in the spacecraft frame, and $\mathbf{v_{sc}}$: the spacecraft velocity), the axial component of $\mathbf{E}_\perp$ can be calculated from $\mathbf{v_{drift}}$ using the MHD assumption.

[15] In addition the new tool transforms from spacecraft-velocity-based coordinates to north-south, east-west coordinates for analyzing the morphology and structure of the auroral return current region more effectively. Details of the numerical method for the coordinate transformation are given in Appendix A.

3. Data Examples

[16] We will consider three separate case studies showing examples of differing spatial structures for return current region potential structures. We define a sheetlike structure of $\mathbf{E}_\perp$ as that for which the ratio of the two components of

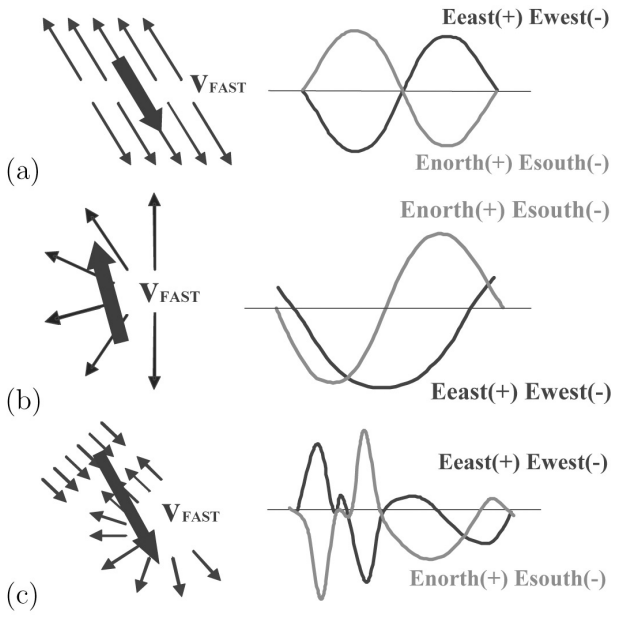

Figure 3. Cartoon illustrations of $\mathbf{E}_\perp$ signatures from crossings of differently shaped potential structures. The thin arrows show the electric field, and the thick arrow the spacecraft velocity. (a) The first example shows a sheetlike case; (b) the second is curved; and (c) the third is changing.

perpendicular electric field remains constant as the spacecraft crosses the structure and call the corresponding potential structures sheetlike potential structures. It should be noted that a criteria of constant ratio is somewhat subjective since it is based on visual inspection of hodograms and time plots. We use similar terminology for the cases where the ratio of two components of $\mathbf{E}_\perp$ varies across the structure, defining them as curved structures of $\mathbf{E}_\perp$ and the corresponding potential structures as curved potential structures. These rotating electric field vector events could be representative of either filamentary potential structures or curves in otherwise sheetlike structures where the ratios of curvature are comparable to the thickness. Rather than saying "curved or filamentary" throughout the text, we refer to these events as simply "curved." It should be noted that the events studied here are interpreted as predominantly regions of downward sheet current (sometimes curved), and either "sheetlike" or "curved" potential structures are embedded within them.

[17] Figure 3 illustrates in cartoon form the relationship between the shape of the potential and field structures, and the corresponding $\mathbf{E}_\perp$ measurement signatures. The distinction between sheetlike and curved signatures is important, as curved structures require gradients in an additional direction. Sheetlike structures can be interpreted as straight arcs; curved structures require gradients along the arc.

3.1. Example 1: Sheetlike Structure, Orbit 1750

[18] Column one of Figure 4 shows a typical example of a sheetlike $\mathbf{E}_\perp$ signature, from FAST orbit 1750, during 12 s starting from 4102 UT. The spacecraft was passing southward over the northern hemisphere, near the morning sector, at altitudes near 3400 km.

[19] Figure 4a shows the variation of the magnetic field perpendicular to the spacecraft trajectory and Figures 4b to 4e show spectrograms of upgoing electron energy, electron pitch angle, ion energy, and ion pitch angle. Where upgoing energetic electron beams from below the spacecraft are found, the positive slope of $\delta\mathbf{B}$ in the spacecraft frame implies that these beams are associated with a downward current region.

[20] Figure 4f shows the spin-axis component of perpendicular electric field calculated from ion distributions, while Figure 4g shows the spin-plane component observed by FAST field measurements. (The label "$\mathbf{E_{av}}$" denotes "electric field-along-velocity vector" for the component of $\mathbf{E}_\perp$ in the trajectory (spin) plane.) The electric field instrument measurements (30 μs) have been filtered to the same sampling time as the ion-spectra-derived measurements (78 ms). The light blue line in Figure 4f indicates the spacecraft velocity contribution. Figure 4h shows these two components transformed from spacecraft coordinates to east (black, positive)-west (black, negative), north (red, positive)-south (red, negative) coordinates. Figure 4i shows $\delta\mathbf{B}$ (the magnetic fluctuation perpendicular to the geomagnetic field, $\mathbf{B_0}$) in the same coordinates, with black indicating the north-south component of $\delta\mathbf{B}$ and red the east-west component. In Figure 4j, upgoing electron characteristic energy (the ratio of energy flux to number flux) is compared to the electric potential (red) calculated from $-\int \mathbf{E} \cdot d\mathbf{l}$ [*Carlson et al.*, 1998a; *Jasperse*, 1998]. The bottom panel shows Poynting fluxes carried by the perpendicular electric and magnetic fields. The contribution of $\mathbf{E_{east}} \times \delta\mathbf{B_{north}}$ is shown in blue and that of $\mathbf{E_{north}} \times \delta\mathbf{B_{east}}$ in red, and black is the sum of both contributions. Positive values correspond to upward flux.

[21] Near 4108 UT, there are intense ion energy fluxes and an asymmetry in the ion pitch angle patterns. The two perpendicular electric field components during this short time period show fairly strong (up to 1100 mV/m) DC fields, and very well correlated bipolar signatures, in the northwest to the southeast direction. These sheetlike bipolar diverging $\mathbf{E}_\perp$ are consistent with a longitudinally extended U-shaped quasi-static potential picture, as typified in Figure 3a. The two components of $\mathbf{E}_\perp$, seen as the spacecraft crosses the structure, give information about the geometry of the potential structure. In this example a slight imbalance in the magnitudes of $\mathbf{E}_\perp$ between the first and second halves of the event (the ratio of the two components of perpendicular electric field remains the same) can be explained by the illustration in Figure 5a.

3.2. Example 2: Curved Structure: Orbit 1626

[22] Figure 4b shows a typical example of a curved $\mathbf{E}_\perp$ structure, from FAST orbit 1626, during 17 s starting from 0735 UT. The spacecraft was passing northward over the northern hemisphere, near midnight, at altitudes above 4000 km. Again the positive slope in the variations of magnetic field ($\delta\mathbf{B}$) indicates a downward current region. Where the most strongly asymmetric patterns in the ion pitch angle spectrum are found near 0745 UT, intense field events (up to 1100 mV/m) are observed.

[23] The $\mathbf{E}_\perp$ of orbit 1626 have a distinctive difference from orbit 1750 in that the east-west components (black) are unipolar whereas the north-south components (red) are

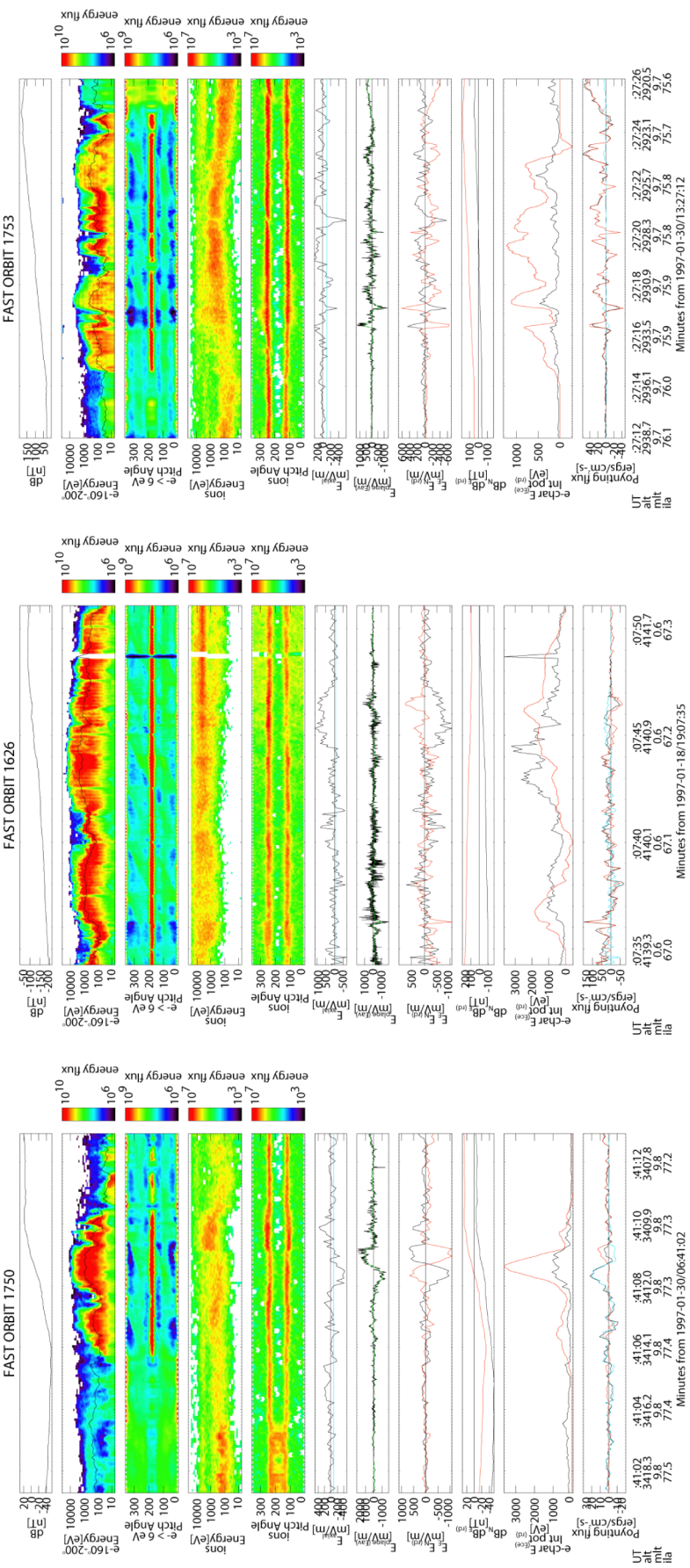

Figure 4. (A) Sheetlike event, from FAST orbit 1750, (B) curved event, from FAST orbit 1626, (C) changing event, from FAST orbit 1753. Panels: (a) The spin-axial magnetic field variation along $\hat{\mathbf{Q}}$ direction, $\mathbf{Q}$ defined in Appendix A, (b) upgoing electron energy spectrogram, (c) electron pitch angle spectrogram, (d) ion energy spectrogram, (e) ion pitch angle spectrogram, (f) the spin-axial component of $E_\perp$ calculated from ion distributions, (g) the spin-plane component of $\mathbf{E}_\perp$, "E-along-velocity" observed by FAST field measurements, (h) the two $\mathbf{E}_\perp$ components transferred to the geographic coordinates (black: east-west, red: north-south components), (i) two $\delta\mathbf{B}$ components in the geographic coordinates, (j) upgoing electron characteristic energy (the ratio of energy flux to number flux, black) with the electric potential calculated from integrating $\mathbf{E}_\perp$ along FAST trajectory (red), and (k) Poynting flux (blue: $\mathbf{E}_{\mathbf{east}} \times \delta\mathbf{B}_{\mathbf{north}}$, red: $\mathbf{E}_{\mathbf{north}} \times \delta\mathbf{B}_{\mathbf{east}}$, and black: the sum of both contributions.)

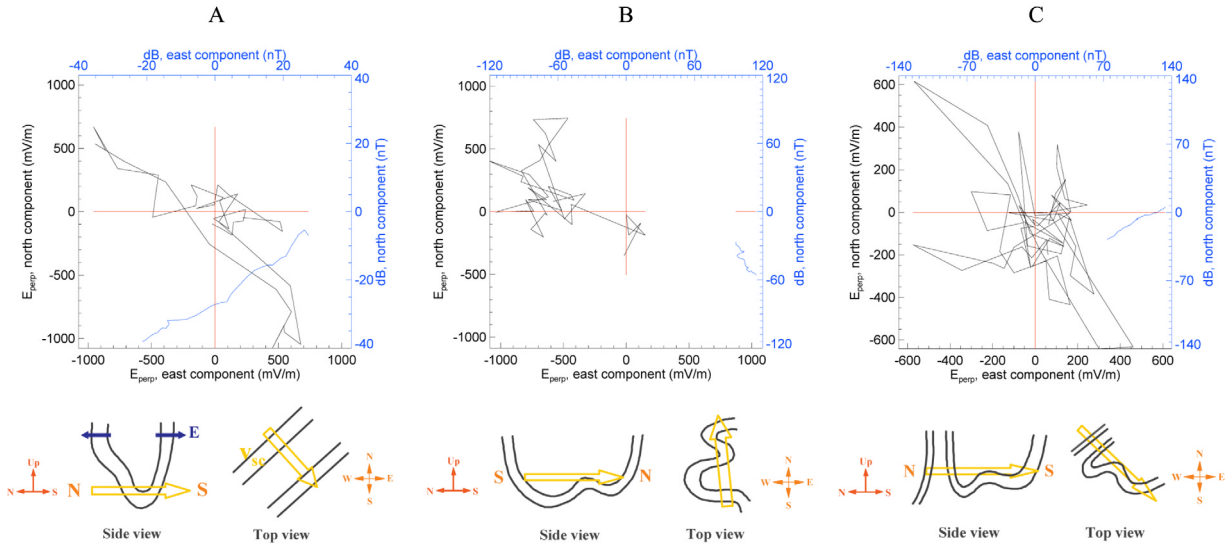

Figure 5. Hodograms and geometric illustrations for case study events from (a) orbit 1750, (b) orbit 1626, and (c) orbit 1753. Each hodogram plots the two perpendicular components of the fields against each other (black: $\mathbf{E}_\perp$, blue: $\delta\mathbf{B}$, horizontal: east, vertical: north).

bipolar. In a one dimensional picture (perpendicular to **B**), unipolar $\mathbf{E}_\perp$ are interpreted as S-shaped quasi-static potential structures, and bipolar as U-shaped potential structures [*Marklund et al.*, 1997; *Karlsson et al.*, 2004]. In this example, the east-west components are totally westward during the strong electric field event while the north-south components vary from southward to northward during the same period. Here we clearly need two dimensions in the perpendicular **B** plane to interpret these signatures, which can be interpreted as the spacecraft passing through the western edge of a quasi-static potential structure elongated in the east-west direction. Another possibility is a local vortex structure in the perpendicular plane, often observed in auroral spirals and surges, as proposed by early Freja measurements [*Marklund et al.*, 1994].

[24] Alternatively this signature could be caused by a time-varying sheetlike structure, but statistical arguments weigh against this interpretation [*Hwang et al.*, 2006]. Assuming a quasi-static potential structure, its probable geometry is illustrated in Figure 5b.

3.3. Example 3: Changing Structure: Orbit 1753

[25] Figure 4c shows a changing structure of $\mathbf{E}_\perp$, from FAST orbit 1753. Again intense upflowing electron fluxes are observed to be coincident with energetic ion conics with asymmetric pitch angle distributions. The positive slope of $\delta\mathbf{B}$ indicates a downward current region.

[26] Two adjacent downward current channels are observed from 1327:16 UT to 1327:19 UT, with the spacecraft passing though in the southward direction. The most intense fields (up to 650 mV/m) are seen to be sheetlike structured in the first current channel near 1327:16–1327:17 UT followed by a weaker curved structured $\mathbf{E}_\perp$ at 1327:18 UT. A possible geometry is shown in Figure 5c.

3.4. Hodograms

[27] Another way to visualize the $\mathbf{E}_\perp$ structure is to plot the components in a hodogram format. These hodograms illustrate clearly the sheetlike and curved structures in the format typically used to illustrate the polarization of wave fields. Corresponding hodograms can be made for $\delta\mathbf{B}$. Figure 5 shows the case studies described above as hodograms for both $\mathbf{E}_\perp$ and $\delta\mathbf{B}$.

[28] Figure 5a shows hodogram for the event of Figure 4a. The hodogram of this sheetlike structure shows a clear, linear polarization in this format, and looks like the polarized $\mathbf{E}_\perp$ of a linear oscillation.

[29] The $\delta\mathbf{B}$ hodogram is overplotted in blue. It is also linear, and is perpendicular to the $\mathbf{E}_\perp$ trace. The relationship between $\mathbf{E}_\perp$ and $\delta\mathbf{B}$ is such that the Poynting fluxes carried by these fields are predominantly upward from the lower ionosphere to the magnetosphere, as shown in panel (k) of Figure 4a.

[30] A probable equipotential structure for this event is shown in the bottom of Figure 5a. The left cartoon shows a side view of the structure along the spacecraft trajectory and the right one is the view from above. Since the equatorial leg of the U-shaped potential is enhanced a bit, the equipotential structure is steeper on that side.

[31] Figure 5b shows the $\mathbf{E}_\perp$ event from orbit 1626 (Figure 4b) which was interpreted as a curved structure. During the interval of interest, the $\mathbf{E}_\perp$ vector rotates clockwise in the hodogram. The corresponding $\delta\mathbf{B}$ hodogram shows a variable curved shape as well, and has no clear correlation to the $\mathbf{E}_\perp$ hodogram pattern.

[32] The Poynting fluxes carried by these two fields are directed weakly upward during the first three quarters of the event; later near 1907:46–1907:47 UT, a strong downward Poynting flux is observed. A schematic illustration at the bottom of Figure 5b shows its probable potential geometry. The bipolar north-south component near 1907:46 UT corresponds to a small ridge in the equipotential surfaces.

[33] Figure 5c shows the hodogram corresponding the changing $\mathbf{E}_\perp$ event of orbit 1753 (Figure 4c). Two linear sectors from southeast to northwest are followed by a weaker clockwise rotating $\mathbf{E}_\perp$. The corresponding $\delta\mathbf{B}$ hodogram shows a fairly straight line which is perpendi-

cular to the linear $\mathbf{E}_\perp$ trace when sheetlike structure is observed. The $\delta\mathbf{B}$ signature is irregular and gently curved when a curved $\mathbf{E}_\perp$ is dominant later. The first linear $\mathbf{E}_\perp$ sector is directed to the southeast direction while the corresponding $\delta\mathbf{B}$ vector points southeast to east, resulting in upward Poynting fluxes carried by these two fields. The second linear $\mathbf{E}_\perp$ sector, which is in the northwest direction, is coincident with an eastward $\delta\mathbf{B}$ vector, resulting in downward Poynting fluxes as shown in panel k of Figure 4c.

[34] A possible potential structure illustrated in Figure 5c shows a rippling shape. Two linear $\mathbf{E}_\perp$ peaks near 1327:16 UT to 1327:17 UT correspond to the steep equipotential structures since the scale size is small. Prior to the first peak, small magnitude, irregular $\mathbf{E}_\perp$ profiles correspond to a gentle, spreading shape of equipotential structures which do not contribute to the large perpendicular electric fields, but induce intense upgoing electron fluxes as shown in panel b and c of Figure 4c. After the second peak, a curved $\mathbf{E}_\perp$ corresponds to a curved potential structure which appears as a curve from the top.

4. Statistical Analysis

[35] A total of 71 examples from 50 FAST orbit were collected based on the occurrence of strong (>100 mV/m) perpendicular electric field events in downward current regions at altitudes from 2500 km to 4100 km from, either the prenoon dayside or near midnight local time regions.

[36] These 71 events are classified as sheetlike or curved based on the definitions of section 3. Among these 71 downward crossings of FAST, 35 passes showed curved events and 25 passes showed sheetlike events. 11 showed changing structure from sheetlike to curved or reverse during a relatively short time period.

[37] Corresponding hodograms of $\delta\mathbf{B}$ tend to be consistent with this classification. For sheetlike cases, hodogram patterns of $\delta\mathbf{B}$ are generally straight during the same time periods as the strong electric field events, indicating sheetlike current structures. For curved events, the $\delta\mathbf{B}$ signature is often also curved, indicating tube-like or curved current structures. However, there are also curved potential events which reside within sheetlike current structures.

[38] The statistical database includes other information about each event as well indicating the scale length of the $\mathbf{E}_\perp$ and the $\delta\mathbf{B}$ structures, and the peak magnitude of $\mathbf{E}_\perp$. The scale length $\mathbf{L}_{\delta\mathbf{B}}$ is taken as the overall extent of the positive slope region of $\delta\mathbf{B}$ (this is sometimes clearer in longer time plots than are shown here). The scale length $\mathbf{L}_{\mathbf{E}_\perp}$ is meant to be the extent of the electric field event, that is, we look for boundaries where the coherent event signatures deviate from the background non-event level. This is a somewhat subjective description but we use the result for only fairly qualitative comparisons. Figure 6 shows scatter plots of the scale length of the $\mathbf{E}_\perp$ structure versus the scale length of the current channel (Figure 6a) and the magnitude of $\mathbf{E}_\perp$ versus the scale length of $\mathbf{E}_\perp$ (Figure 6b). Sheetlike events are shown in red, curved in green, and changing in blue.

[39] Figure 6a shows that the scale length of $\mathbf{E}_\perp$ ($\mathbf{L}_{\mathbf{E}_\perp}$) is always smaller than or equal to the current sheet size of $\mathbf{L}_{\delta\mathbf{B}}$. For large-scale size currents ($\mathbf{L}_{\delta\mathbf{B}}$ > 100 km) more of the $\mathbf{E}_\perp$ events are curved. Both sheetlike and curved events appear for the small (<100 km) scale length current structures.

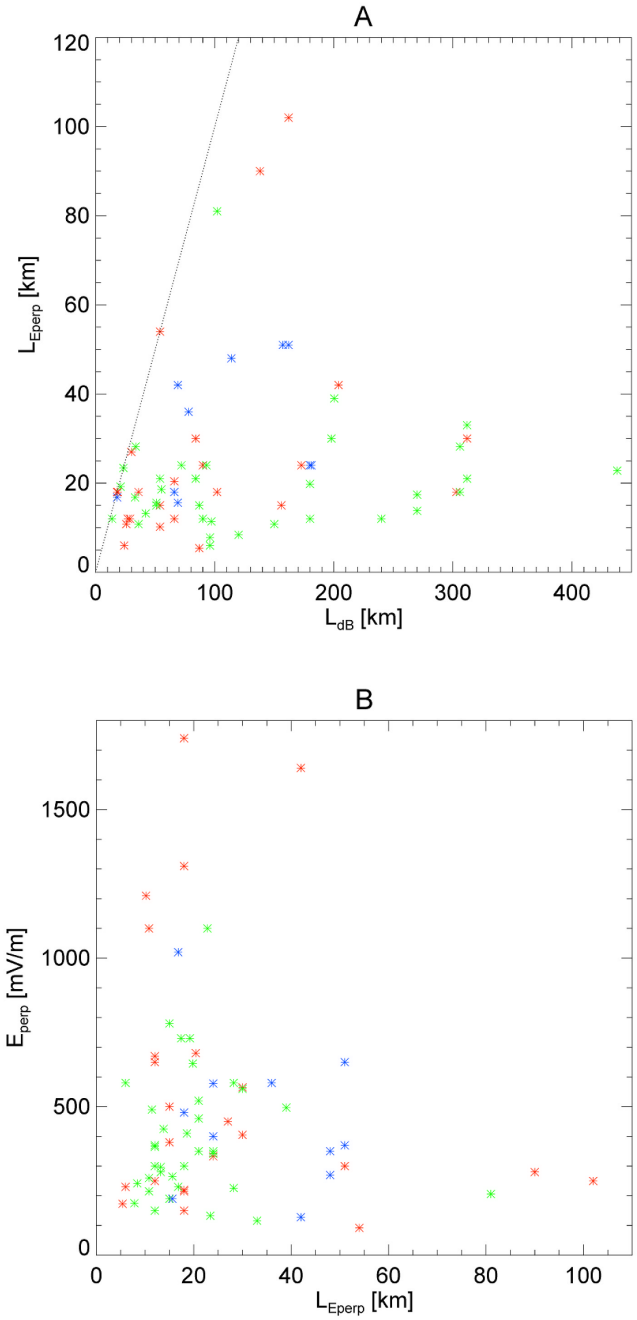

Figure 6. Scatterplots for (a) the scale length of current channel $\mathbf{L}_{\delta\mathbf{B}}$ versus the scale length of electric field structure $\mathbf{L}_{\mathbf{E}_\perp}$, and (b) the scale length of electric field structure $\mathbf{L}_{\mathbf{E}_\perp}$ vs. magnitude of the perpendicular electric field $\mathbf{E}_\perp$.

[40] Figure 6b shows that the relationship between scale length of $\mathbf{E}_\perp$ and magnitude of $\mathbf{E}_\perp$ varies with the structural signatures. Sheetlike events (red) show a reciprocal relation between them, and curved cases (green) show a weakly proportional relation. Thus a stronger sheetlike $\mathbf{E}_\perp$ has a narrower scale length, and a stronger curved $\mathbf{E}_\perp$ has a broader scale length. It is interesting to note, however, that both curved and sheetlike events cover roughly the same range of scales of $\mathbf{L}_{\mathbf{E}_\perp}$.

[41] The two diagrams indicate that smaller current sheets and narrow arcs tend towards stronger sheetlike diverging $\mathbf{E}_\perp$ structures. Larger current channels tend towards stronger curved signatures of broad $\mathbf{E}_\perp$ structures. Importantly, though, neither scale size nor magnitude of field signatures can clearly separate sheetlike events from curved. In addition, magnitude of $j_\parallel$ (not shown) does not sort them.

5. Discussion

[42] Return current regions are characterized by upward acceleration of cold ionospheric electrons, perpendicularly heated ions, and diverging electric fields within a current channel, as are seen in our examples. As a counterpart to adjacent upward current regions, U-shaped potentials with downward pointing parallel electric fields have been adopted as an analog of the potential structure for the return current region. They are typically thought to be elongated in a longitudinal direction and pictured as straight black arcs.

[43] We find that curls or curved filamentary structures with curved potential structures are more frequently observed than straight arcs with sheetlike $\mathbf{E}_\perp$ in downward current regions. A significant fraction (35 to 46 out of 71) of the downward current structures in our study have irregular filamentary or curved potential structures such as curls, vortices, folds or ends, and cannot be idealized as straight arcs.

[44] This result is consistent with ground camera images of black auroral arc structures. They are often seen as curved and swirling shapes in the background of bright arcs, rather than as straight structures, though straight black arcs can also be seen. For curved structures, one must consider variations along the arc since the importance of gradients along the arc cannot be negligible for the basic structure of these events.

[45] A statistical comparison of current channel scale length and magnitude of $E_\perp$ indicates that more of the larger current channels (>100 km) show curved potential structure. In contrast, most of the strongest (>1000 mV/m) events show a sheetlike structure in a relatively small scale length of current channel. Sheetlike $E_\perp$ confined to smaller current structures may indicate an earlier stage of current structure evolution, given that some numerical models predict a growing $\mathbf{L}_{\delta\mathbf{B}}$ with time [*Streltsov and Marklund*, 2006].

[46] Statistical scatter plots show that for sheetlike structures the magnitude of $\mathbf{E}_\perp$ and the scale length of the corresponding potential structure are reciprocally related and that for curved structures they are weakly proportional. The fact that the more intense sheetlike $\mathbf{E}_\perp$ are associated with the smaller scale length might indicate that the structures are adjacent to and limited by the upward current structures of bright auroral arcs [*Karlsson and Marklund*, 1996]. However, our data are not generally consistent with this interpretation, showing instead that more intense $\mathbf{E}_\perp$ are not located adjacent to an auroral arc or between two auroral arcs.

[47] In all sheetlike and curved structures, the scale length of $\mathbf{E}_\perp$ (the scale length of the potential structure) is always less than or equal to the scale length of the associated current sheet. FAST frequently observes a series of several narrow potential structures within a single current structure. It has been proposed that there are multiple double layers associated with a series of electron phase space holes (electron solitary structures) along the field line, i.e., multilayered U-shaped potential structures nested within each other along a field line [*Lysak and Dum*, 1983; *Lysak and Hudson*, 1987; *Sato and Okuda*, 1981; *Andersson*, 2002]. In this case a perpendicularly moving spacecraft might see a series of unipolar $\mathbf{E}_\perp$ structures (S-shaped potentials) during the first half of a region and see another series of unipolar $\mathbf{E}_\perp$ of the opposite polarity during the other half. However, FAST observations of arrays of potential structures are always associated with a series of bipolar field signatures, indicating that narrow potential structures are on neighboring field lines along the spacecraft passage.

[48] The scatterplots of section 4 illustrate that sheetlike or curved potential structure is not a clear function of scale size. We show in the companion paper that sheetlike and curved structures are instead clearly separated according to a parameter related to the relative importance of ionospheric fields.

6. Conclusions and Future Work

[49] Using 71 downward current region crossings from FAST, we investigated the potential structure of return current regions. The findings are as follows.

[50] 1. The majority of downward current regions contain curved potential structures rather than straight arcs.

[51] 2. This interpretation is supported by the observed magnetic fluctuations. For curved cases δB is often seen to be curved in a hodogram, indicating a tube-like or curved current channel. For sheetlike cases $\delta\mathbf{B}$ hodograms show a straight line, indicating sheetlike structures which are perpendicular to $\mathbf{E}_\perp$.

[52] 3. The statistics show that the strongest electric field events are sheetlike and the larger current scale sizes tend to contain curved potential structures.

[53] 4. In all cases, the scale length of $\mathbf{E}_\perp$ is smaller than or equal to the scale length of current sheet ($\mathbf{L}_{\mathbf{E}_\perp} \leq \mathbf{L}_{\delta\mathbf{B}}$), and often multiple potential structures are contained in a single current structure.

[54] Given both components of the full DC electric vector, we can study various questions including the morphology of auroral return current regions and inconsistencies with static return current models comparing field and particle signatures. The statistics demonstrate that neither scale sizes of current channel and potential, nor magnitudes of electric field and $j_\parallel$, can clearly distinguish sheetlike cases from curved cases. In a companion paper [*Hwang et al.*, 2006], we proceed with our study to find a crucial factor for distinguishing the different structures and the implications underlying it.

Appendix A: Coordinate Transformation From the Velocity-Based Coordinates to the Northeast $\mathbf{B}_\perp$ – Plane Coordinates

[55] FAST electric field data for the spin-plane components and ion drift moments for the spin-axial components are combined to determine the full DC $\mathbf{E}$ vector. However these two components are calculated in the spacecraft

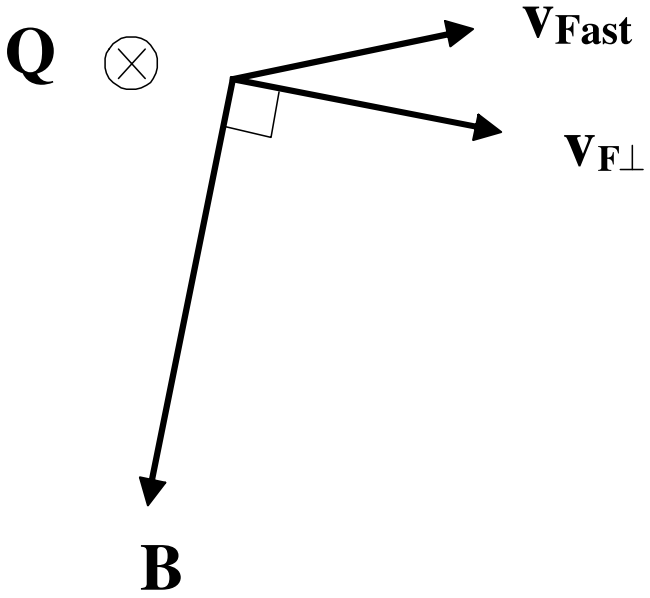

Figure A1. Illustration of coordinate system in the reference frame of spacecraft.

coordinate system which varies slightly with every revolution, causing difficulties for statistical analysis. In order to investigate $\mathbf{E}_\perp$ morphologies more efficiently, we transform the two $\mathbf{E}_\perp$ components from spacecraft-velocity-based coordinates to north-south, east-west geographic coordinates in the plane perpendicular to $\mathbf{B}$.

[56] Figure A1 shows three-dimensional orthogonal coordinates in the frame of a moving spacecraft. We define

$$\mathbf{x-axis}: \hat{\mathbf{v}}_{F\perp} = \frac{\mathbf{v_{F\perp}}}{\| \mathbf{v_{F\perp}} \|}$$

$$\mathbf{y-axis}: \hat{\mathbf{Q}} = \frac{\mathbf{Q}}{\| \mathbf{Q} \|}$$

$$\mathbf{z-axis}: \hat{\mathbf{B}} = \frac{\mathbf{B}}{\| \mathbf{B} \|}$$

$$\mathbf{Q} = \mathbf{v_{Fast}} \times \mathbf{B}$$

$$\mathbf{v_{F\perp}} = \mathbf{B} \times (\mathbf{v_{Fast}} \times \mathbf{B})$$

All three of these unit vectors are easily described in a GEI coordinate system using FAST orbit data.

[57] The ion drift velocity (plasma velocity) in the $\mathbf{v}_{F\perp}$ direction, $(\mathbf{v_D} \cdot \hat{\mathbf{v}}_{\mathbf{F}\perp})\ \hat{\mathbf{v}}_{\mathbf{F}\perp}$ can be obtained from ion moments. The $\hat{\mathbf{Q}}$ component of $\mathbf{v_D}$ is obtained from FAST field data, $\mathbf{E_{alongv}}$ (i.e., the electric field component along the spacecraft trajectory). For northward or southward passages of FAST, $\hat{\mathbf{Q}}$ is westward or eastward. In either case, $\mathbf{E_{alongv}} \times \mathbf{B}$ always points parallel to $\hat{\mathbf{Q}}$ and $\mathbf{E_{alongv}} \times \mathbf{B}$ is what is computed, i.e., $(\mathbf{v_D} \cdot \hat{\mathbf{Q}})\ \hat{\mathbf{Q}} = \frac{\mathbf{E_{alongv}}}{\mathbf{B}}\ \hat{\mathbf{Q}}$. Therefore $\mathbf{v_D}$ is expressed as

$$\mathbf{v_D} = (\mathbf{v_D} \cdot \hat{\mathbf{v}}_{\mathbf{F}\perp})\hat{\mathbf{v}}_{\mathbf{F}\perp} + (\mathbf{v_D} \cdot \hat{\mathbf{Q}})\hat{\mathbf{Q}}$$

The coefficient of the first term is thus obtained from ion data, and the second is from FAST field data.

[58] East and north unit vectors, $\hat{\mathbf{E}}$ and $\hat{\mathbf{N}}$, respectively, are written in GEI coordinates.

$$\hat{\mathbf{E}} = \frac{\hat{\mathbf{z}}_{\mathrm{GEI}} \times \hat{\mathbf{R}}}{\| \hat{\mathbf{z}}_{\mathrm{GEI}} \times \hat{\mathbf{R}} \|} \quad \text{and} \quad \hat{\mathbf{N}} = \frac{\hat{\mathbf{R}} \times \hat{\mathbf{E}}}{\| \hat{\mathbf{R}} \times \hat{\mathbf{E}} \|}$$

[59] What is wanted are $\hat{\mathbf{E}} \cdot \mathbf{v_D}$ (east component of the drift velocity) and $\hat{\mathbf{N}} \cdot \mathbf{v_D}$ (north component of the drift velocity), which are

$$\hat{\mathbf{E}} \cdot \mathbf{v_D} = (\mathbf{v_D} \cdot \hat{\mathbf{Q}})(\hat{\mathbf{E}} \cdot \hat{\mathbf{Q}}) + (\mathbf{v_D} \cdot \hat{\mathbf{v}}_{\mathbf{F}\perp})(\hat{\mathbf{E}} \cdot \hat{\mathbf{v}}_{\mathbf{F}\perp})$$

$$\hat{\mathbf{N}} \cdot \mathbf{v_D} = (\mathbf{v_D} \cdot \hat{\mathbf{Q}})(\hat{\mathbf{N}} \cdot \hat{\mathbf{Q}}) + (\mathbf{v_D} \cdot \hat{\mathbf{v}}_{\mathbf{F}\perp})(\hat{\mathbf{N}} \cdot \hat{\mathbf{v}}_{\mathbf{F}\perp})$$

Using

$$\mathbf{E} = -\mathbf{v_D} \times \mathbf{B} = -\begin{pmatrix} \hat{\mathbf{N}} & \hat{\mathbf{E}} & \hat{\mathbf{z}} \\ \mathbf{v_{D\,north}} & \mathbf{v_{D\,east}} & \mathbf{0} \\ \mathbf{0} & \mathbf{0} & \mathbf{B} \end{pmatrix}$$

the east and north components of $\mathbf{E}_\perp$ are obtained. Therefore this transformation of coordinate systems changes the two components of $\mathbf{E}_\perp$ in the velocity-based coordinates to two components of $\mathbf{E}_\perp$ in north-east $\mathbf{B}_\perp$ coordinates.

[60] **Acknowledgments.** T. Karlsson and J. Clemmons provided Freja data related to the large $E_\perp$ events and helped me interpret their sheetlike and curved structure properties. I also appreciate valuable advice from J. P. McFadden about the study using FAST data. We thank both reviewers and the editor for their thoughtful and constructive comments. This work was supported by NASA grant NAG5-10472 and by Dartmouth College.

[61] Arthur Richmond thanks the reviewers for their assistance in evaluating this paper.

References

Andersson, L. (2002), Characteristics of parallel electric fields in the downward current region of the aurora, *Phys. Plasmas*, *9*, 3600.

Carlson, C. W., et al. (1998a), FAST observations in the downward auroral current region: Energetic upgoing electron beams, parallel potential drops, and ion heating, *Geophys. Res. Lett.*, *25*, 2017.

Carlson, C. W., R. F. Pfaff, and J. G. Watzin (1998b), The fast auroral snapshot (FAST) mission, *Geophys. Res. Lett.*, *25*, 2013.

Chiu, Y. T., and M. Schultz (1978), Self-consistent particle and parallel electrostatic field distributions in the magnetosphere-ionosphere auroral region, *J. Geophys. Res.*, *83*, 629.

Ergun, R. (2001), Electron phase-space holes and the VLF saucer source region, *Geophys. Res. Lett.*, *28*, 3805.

Ergun, R. (2003), Double layers in the downward current region of the aurora, *Nonlinear Proc. Geophys.*, *10*, 45.

Ganguli, G., and P. J. Palmadesso (1988), Electrostatic ion instabilities in the presence of parallel currents and transverse electric fields, *Geophys. Res. Lett.*, *15*, 103.

Hwang, K., K. Lynch, C. Carlson, J. Bonnell, and W. Peria (2006), FAST observations of perpendicular DC electric field structures in downward auroral current regions: Implication, *J. Geophys. Res.*, *111*, A09206, doi:10.1029/2005JA011472.

Jasperse, J. R. (1998), Ion heating, electron acceleration, and the self-consistent parallel E-field in downward auroral current regions, *Geophys. Res. Lett.*, *25*, 3485.

Johansson, T., and G. Marklund (2005), Electric fields signatures at density gradients, *Eos Trans. AGU*, *86*(52), Fall Meet. Suppl., Abstract SM41B–1179.

Karlsson, T., and G. T. Marklund (1996), A statistical study of intense low-altitude electric fields observed by Freja, *Geophys. Res. Lett.*, *23*, 1005.

Karlsson, T., G. Marklund, S. Figueiredo, T. Johansson, and S. Buchert (2004), Separating spatial and temporal variations in auroral electric and magnetic fields by Cluster multipoint measurements, *Ann. Geophys.*, *22*, 2464.

Lynch, K. A., J. W. Bonnell, C. W. Carlson, and W. J. Peria (2002), Return current region aurora: $E_{||}$, j_z, particle energization and BBELF

wave activity, *J. Geophys. Res.*, *107*(A7), 1260, doi:10.1029/2001JA900124.
Lysak, R. L. (1985), Auroral electrodynamics with current and voltage generators, *J. Geophys. Res.*, *90*, 4178.
Lysak, R. L., and C. T. Dum (1983), Dynamics of magnetosphere-ionosphere coupling including turbulent transport, *J. Geophys. Res.*, *88*, 365.
Lysak, R. L., and M. K. Hudson (1987), Effect of double layers on magnetosphere-ionosphere coupling, *Laser Particle Beams*, *5*, 351.
Marklund, G., L. Blomberg, C. Falthammar, and P. Lindqvist (1994), On intense diverging electric fields associated with black aurora, *Geophys. Res. Lett.*, *21*, 1859.
Marklund, G., T. Karlsson, and J. Clemmons (1997), On low altitude particle acceleration and intense electric fields and their relationship to black aurora, *J. Geophys. Res.*, *102*, 17,509.
Marklund, G. T., et al. (2001), Temporal evolution of acceleration structures in the auroral return current region, *Nature*, *414*, 724.
Sato, T., and H. Okuda (1981), Numerical similuations on ion acoustic double layers, *J. Geophys. Res.*, *86*, 3357.
Streltsov, A. V., and G. T. Marklund (2006), Divergent electric fields in the downward current channels, *J. Geophys. Res.*, *111*, A07204, doi:10.1029/2005JA011196.

J. W. Bonnell and C. W. Carlson, Space Sciences Laboratory, University of California, Berkeley, CA 94720, USA. (jbonnell@ssl.berkeley.edu; cwc@ssl.berkeley.edu)
K.-J. Hwang and K. A. Lynch, Department of Physics and Astronomy, Dartmouth College, 6127 Wilder Laboratory, Hanover, NH 03755, USA. (kyoung-joo.hwang@dartmouth.edu; kristina.lynch@dartmouth.edu)
W. J. Peria, Department of Geophysics, University of Washington, Box 351310, Seattle, WA 98195, USA. (peria@ess.washington.edu)